


## Article

# Solvothermal Preparation of a Lanthanide Metal-Organic Framework for Highly Sensitive Discrimination of Nitrofurantoin and L-Tyrosine

Tian-Tian Wang<sup>1</sup>, Jing-Yi Liu<sup>1</sup>, Rui Guo<sup>1</sup>, Jun-Dan An<sup>1</sup>, Jian-Zhong Huo<sup>1</sup>, Yuan-Yuan Liu<sup>1</sup>, Wei Shi<sup>2,\*</sup>  and Bin Ding<sup>1,\*</sup>

- <sup>1</sup> Key Laboratory of Inorganic-Organic Hybrid Functional Material Chemistry, College of Chemistry, Tianjin Normal University, 393 Binshui West Road, Tianjin 300387, China; tiantianwang0912@163.com (T.-T.W.); liujingyi9803@163.com (J.-Y.L.); guoruigrace@163.com (R.G.); sl0729an@163.com (J.-D.A.); hxxylhjz@tjnu.edu.cn (J.-Z.H.); liuyuanliu1973@aliyun.com (Y.-Y.L.)
- <sup>2</sup> Department of Chemistry and Key Laboratory of Advanced Energy Materials Chemistry, College of Chemistry, Nankai University, Tianjin 300071, China
- \* Correspondence: shiwei@nankai.edu.cn (W.S.); hxxymb@tjnu.edu.cn (B.D.)

**Abstract:** Metal-organic frameworks (MOFs) have been rapidly developed for their broad applications in many different chemistry and materials fields. In this work, a multi-dentate building block 5-(4-(tetrazol-5-yl)phenyl)-isophthalic acid (H<sub>3</sub>L) containing tetrazole and carboxylate moieties was employed for the synthesis of a two-dimensional (2D) lanthanide MOF [La(HL)(DMF)<sub>2</sub>(NO<sub>3</sub>)] (DMF = *N,N*-dimethylformamide) (**1**) under solvothermal condition. The fluorescent sensing application of **1** was investigated. **1** exhibits high sensitivity recognition for antibiotic nitrofurantoin ( $K_{sv}$ :  $3.0 \times 10^3 \text{ M}^{-1}$  and detection limit: 17.0  $\mu\text{M}$ ) and amino acid L-tyrosine ( $K_{sv}$ :  $1.4 \times 10^4 \text{ M}^{-1}$  and detection limit: 3.6  $\mu\text{M}$ ). This work provides a feasible detection platform of 2D MOFs for highly sensitive discrimination of antibiotics and amino acids.

**Keywords:** metal-organic frameworks; fluorescence; fluorescent probe; antibiotics; amino acid



**Citation:** Wang, T.-T.; Liu, J.-Y.; Guo, R.; An, J.-D.; Huo, J.-Z.; Liu, Y.-Y.; Shi, W.; Ding, B. Solvothermal Preparation of a Lanthanide Metal-Organic Framework for Highly Sensitive Discrimination of Nitrofurantoin and L-Tyrosine. *Molecules* **2021**, *26*, 3673. <https://doi.org/10.3390/molecules26123673>

Academic Editor: Mei Pan

Received: 14 May 2021  
Accepted: 8 June 2021  
Published: 16 June 2021

**Publisher's Note:** MDPI stays neutral with regard to jurisdictional claims in published maps and institutional affiliations.



**Copyright:** © 2021 by the authors. Licensee MDPI, Basel, Switzerland. This article is an open access article distributed under the terms and conditions of the Creative Commons Attribution (CC BY) license (<https://creativecommons.org/licenses/by/4.0/>).

## 1. Introduction

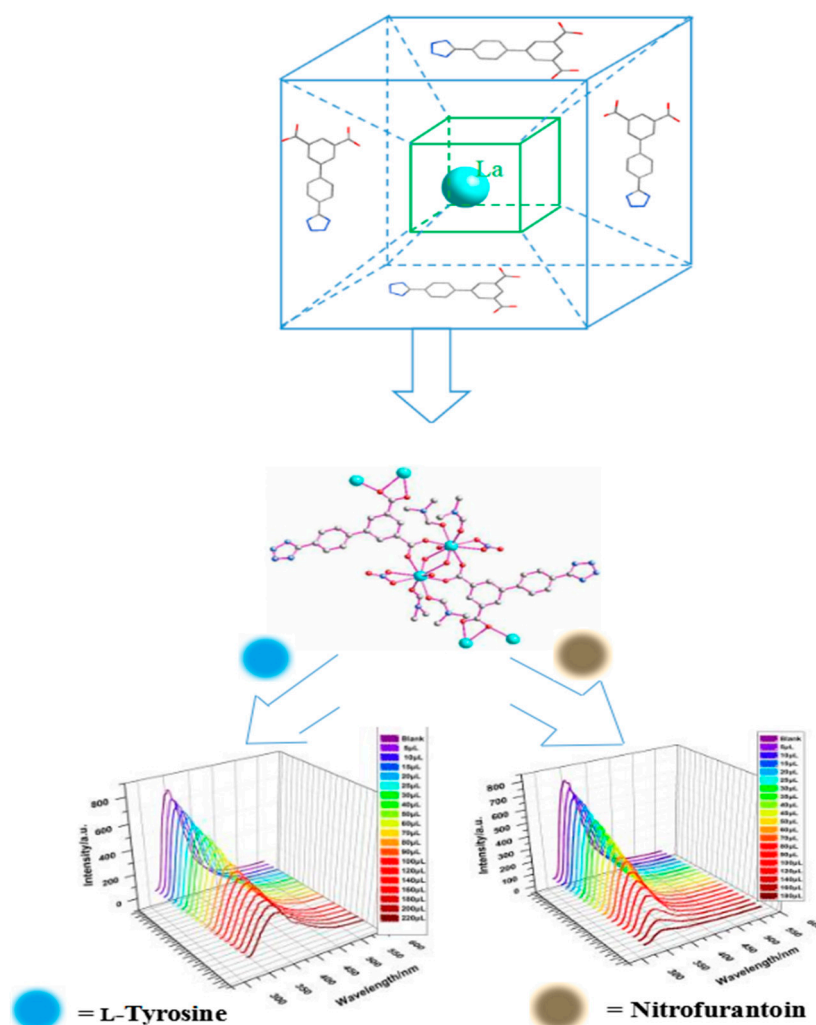
Metal-organic frameworks (MOFs) are coordination compounds with open-framework structure. In the past few decades, MOFs have been widely studied in many fields such as gas storage and separation, adsorption and separation of small chemical species, sensing, catalysis and drug delivery [1–6]. By improving the synthesis method, adjusting the proportion of metal salts, ligands and solvents, and changing the pore structures or porosities, the catalytic, gas adsorption and separation or fluorescence performance can be optimized [7–9]. MOFs can be used as chemical sensors because the interactions between MOFs and analytes could influence their luminescent properties [10–12]. Usually, the chemical sensors could have a “turn on” or “turn off” response to small molecules [13–15]. The characteristic of a good sensor is usually summarized as “4S”: sensitivity, selective, stability and speed of response [16–22].

Since antibiotics were discovered, these molecules have showed applications for disease cure. However, antibiotic pollution has become more and more serious, which is caused by the abuse of antibiotics [23–25]. Nitrofurantoin is an antibiotic that is widely used in the prevention and treatment of animal infectious diseases [26,27], but it has been banned in many countries because of its carcinogenicity and mutagenicity. In 2008, the Ministry of Agriculture of China set the maximum limit of nitrofurantoin in aquatic products at 0.5  $\mu\text{g}/\text{kg}$  [28].

On the other hand, L-tyrosine is an essential amino acid. The deficiency of L-tyrosine may cause phenylketonuria (PKU) [29,30]. PKU is an inborn metabolic error that prevents the conversion of L-tyrosine, causing damage to the central nervous system [31,32]. In

addition, L-tyrosine is associated with dopamine (associated with Parkinson's disease), norepinephrine and epinephrine synthesis [33].

Based on the above consideration, we are interested in developing fluorescent probes for both nitrofurantoin and L-tyrosine [34–36]. In this work, 5-(4-(tetrazol-5-yl)phenyl)-isophthalic acid ( $H_3L$ ) containing tetrazole and carboxylate moieties was employed as a bridging ligand. Through the solvothermal method, a lanthanide MOF,  $[La(HL)(DMF)_2(NO_3)]$  (**1**) was synthesized. We investigated the photo-luminescence sensing performance of **1**, which showed highly sensitive sensing function for both nitrofurantoin ( $K_{SV}$ :  $3.0 \times 10^3 M^{-1}$  and detection limit:  $17.0 \mu M$ ) and L-tyrosine ( $K_{SV}$ :  $1.4 \times 10^4 M^{-1}$  and detection limit:  $3.6 \mu M$ ) with high quenching efficiency and low detection limit (Scheme 1).



**Scheme 1.** Preparation of the lanthanide metal-organic framework for highly sensitive discrimination of nitrofurantoin and L-tyrosine.

## 2. Results and Discussion

### 2.1. Structural Description of **1**

**1** belongs to monoclinic space group  $C2/c$ . As shown in Figure 1a, the asymmetric unit of **1** consists of one  $La^{III}$  center (La1), one de-protonated  $HL^-$ , two mono-coordinated DMF and one bi-coordinated  $NO_3^-$ . The  $HL^-$  ligand serves as a  $\mu_4$ -bridge to link four La centers by a  $\mu_4-\eta^1:\eta^1:\eta^1:\eta^2$  coordination mode through four carboxylate oxygen atoms (O1, O2, O3 and O4). Two DMF molecules are mono-coordinated to La1 through the terminal oxygen atoms (O8 and O9). Besides, two oxygen atoms (O5 and O6) from the nitrate ion are coordinated to La1 forming a bidentate chelating coordination mode [37,38]. The

bond lengths of La-O are in the range of 2.443(2)–2.741(2) Å. The angle range of O-La-O is 72.49(7)–151.40(8)°. All the bond lengths and angles fell into the normal range.

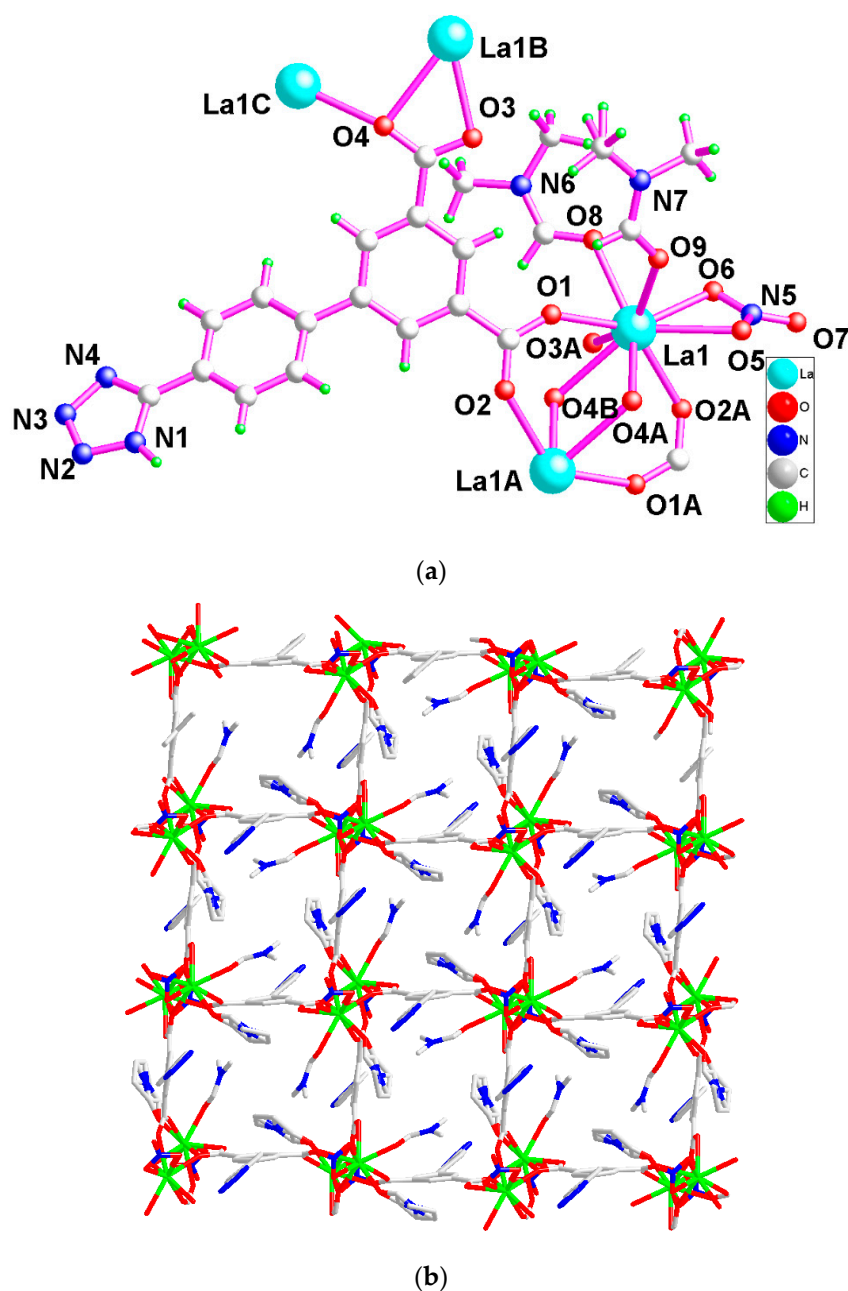


**Figure 1.** (a) The fundamental structure of **1** (symmetry codes: A  $0.5 - x, 1.5 - y, 1 - z$ ; B  $x, 1 - y, 0.5 + z$ ; C  $x, 1 - y, 0.5 + z$ ); (b) two-dimensional framework of **1**.

Figure 1b shows that two neighboring lanthanide atoms (La1A and La1B) are connected by the carboxylate oxygen atoms (O3 and O4) of  $\text{HL}^-$  forming a binuclear building block. The intermetallic distance of La1A and La1B is 4.1258(4) Å. These binuclear building blocks are further linked through  $\text{HL}^-$  to form a two-dimensional network. It is noted that the tetrazole group of  $\text{HL}^-$  is not coordinated and protruded out of the two-dimensional network. There are hydrogen bonding interactions between the two-dimensional networks: N(1)–H(1)···O(5), 2.9651(1) Å and C(3)–H(3)···O(7), 3.3256(1) Å. The hydrogen-bonding interactions further assemble the two-dimensional networks into a three-dimensional supramolecular structure [39].

## 2.2. PXRD, FT-IR and SEM Characterizations of **1**

The powder X-ray diffraction (PXRD) pattern of **1** is shown in Figure 2a. The experimental peaks are consistent with the theoretical one obtained by single-crystal X-ray data [40–42]. We also investigated the stability of **1** in different solvents such as ethanol, DMF and DMA. After 24 h soaking **1** in these solvents, the experimental PXRD patterns of **1** were also consistent with theoretical pattern, indicating that **1** was stable in these solvents (Figure 2b). The slight variation of diffraction intensity may be related to the different crystal orientation or solvent effects [43,44].

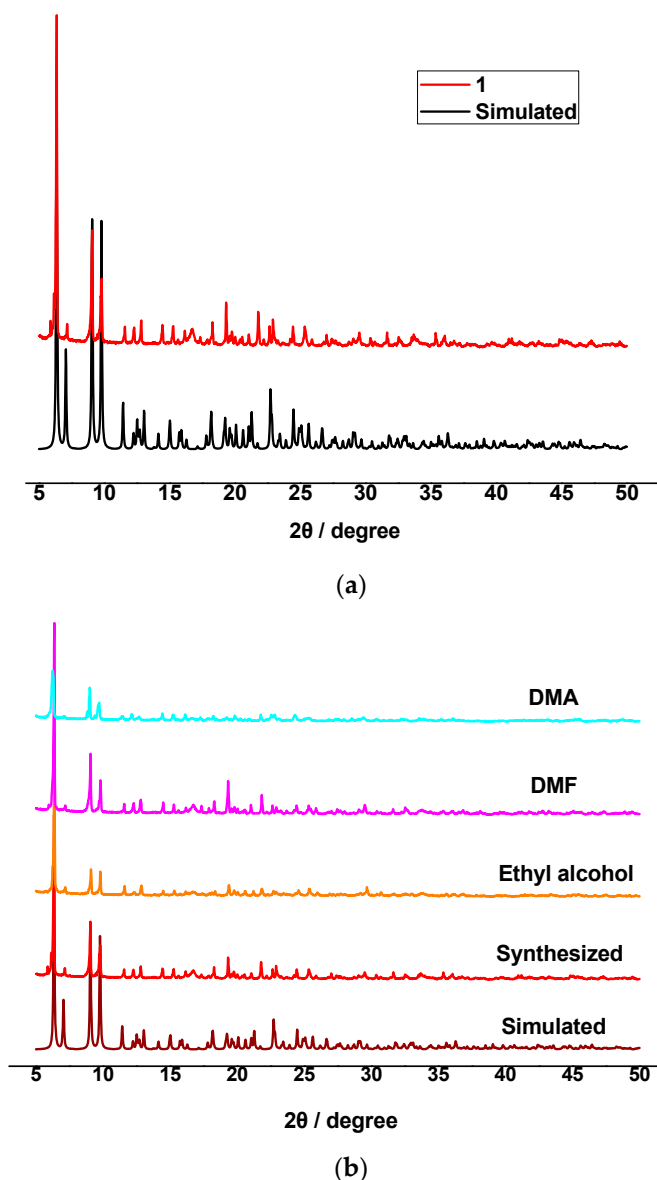


**Figure 2.** (a) PXRD patterns of **1**; (b) PXRD patterns of **1** soaked in different solutions for 24 h.

FT-IR spectrum of **1** in the range of  $4000\text{--}400\text{ cm}^{-1}$  was measured (Figure S1, Supplementary Materials). The strong and wide peak close to  $3412\text{ cm}^{-1}$  can be ascribed to the presence of N–H stretching vibration. The strong peaks of carboxyl groups appear in the region of  $1648\text{--}1584\text{ cm}^{-1}$  (antisymmetric stretching vibrations) and  $1384\text{--}1420\text{ cm}^{-1}$  (symmetric stretching vibrations) [45–47]. No FT-IR peaks around  $1700\text{ cm}^{-1}$  also demonstrated complete deprotonation of carboxyl groups [48–52]. The peaks located at  $1499\text{ cm}^{-1}$  are from the tetrazole group. The band located at  $1296\text{ cm}^{-1}$  can be ascribed to the vibration

of C–N [53–55]. The vibration bands from  $779\text{ cm}^{-1}$  to  $719\text{ cm}^{-1}$  are from the aromatic benzene rings.

The morphology of **1** was also investigated by the scanning electron microscope (SEM) [56–62]. As shown in Figure 3a,b, **1** has a blocky morphology with a length of  $54.94\text{ }\mu\text{m}$  and a width of  $21.38\text{ }\mu\text{m}$  [63–67], which is different to that of  $\text{H}_3\text{L}$  (Figure S2a,b, Supplementary Materials) under the same scale.

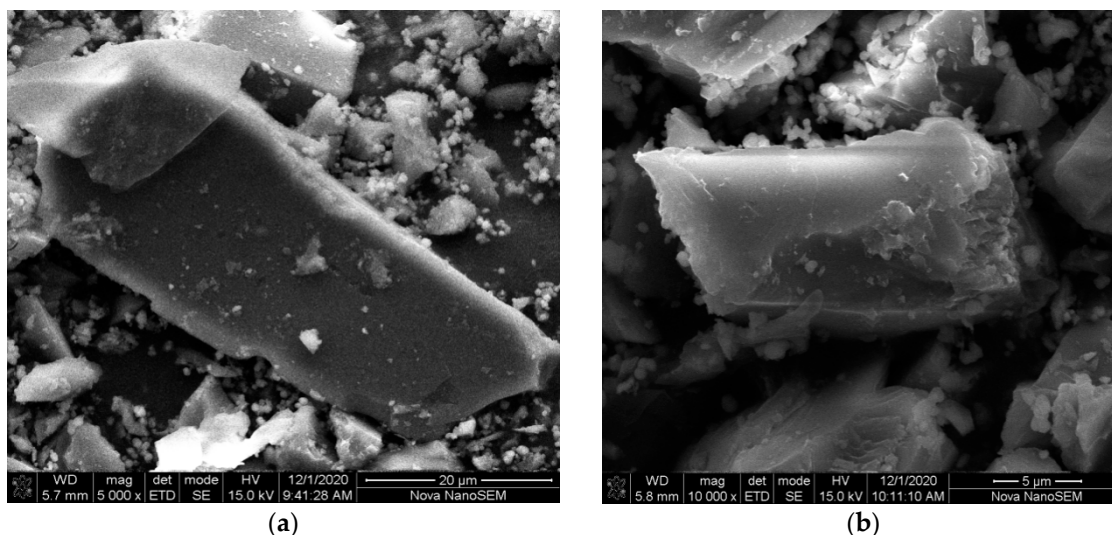


**Figure 3.** (a) The SEM image of **1** at a scale of  $20\text{ }\mu\text{m}$ ; (b) The SEM image of **1** at a scale of  $5\text{ }\mu\text{m}$ .

### 2.3. Photo-Luminescent Properties of **1**

It is well known that luminescence can be divided into two basic modes according to the spin state of electrons during radiation relaxation: fluorescence and phosphorescence [68–70]. The origin of lanthanide MOFs can be mainly ascribed to four kinds of mechanisms listed below: (1) the luminescence based on the organic ligand, (2) the luminescence based on metal center, (3) the luminescence based on the charge transfer, and (4) the luminescence based on guest emission. Lanthanide metal ions contain 4f electrons shielding by  $5s^25p^6$  orbits, which is hardly perturbed by its chemical surroundings, which enable lanthanide ions to have good optical performance [71–73].

UV-Vis spectra of  $\text{H}_3\text{L}$  and **1** were measured at room temperature (Figure S3, Supplementary Materials). The maximum absorption peak positions of  $\text{H}_3\text{L}$  and **1** were different, which can be ascribed to the coordination between  $\text{H}_3\text{L}$  and the metal center. Solid-state fluorescence spectra of  $\text{H}_3\text{L}$  and **1** were also measured, as shown in Figure S4, Supplementary Materials. The peak value of **1** appeared at the same wavelength of  $\text{H}_3\text{L}$  excited at 300 nm, indicating that the fluorescence emission of **1** is from the ligand [74–76].

In order to explore different photo-luminescence responses to antibiotics [77,78], the powder of **1** was evenly distributed in ethanol solution with a concentration of  $0.1\text{ mg/mL}$  by the ultrasonic method at room temperature (ultrasonic power: 100 W; ultrasonic time: 20 min). The antibiotics used are listed below: nitrofurantoin (NFT), ronidazole (RNZ), furazolidone (FZD), nitrofurazone (NFZ), dimetridazole (DMZ), ornidazole (ORN), thiamphenicol (THI), metronidazole (MDZ), chloramphenicol (CHL), sulfamethazine (SMZ) and sulfadiazine (SDZ). In the fluorescence detection experiments, different antibiotics with the concentration of  $0.001\text{ mol/L}$  were added to the 3 mL suspended solutions containing **1**, drop by drop. The fluorescence quenching results are shown in Figure 4a. The results show that the quenching efficiency is different, among which NFT shows the most obvious quenching result.

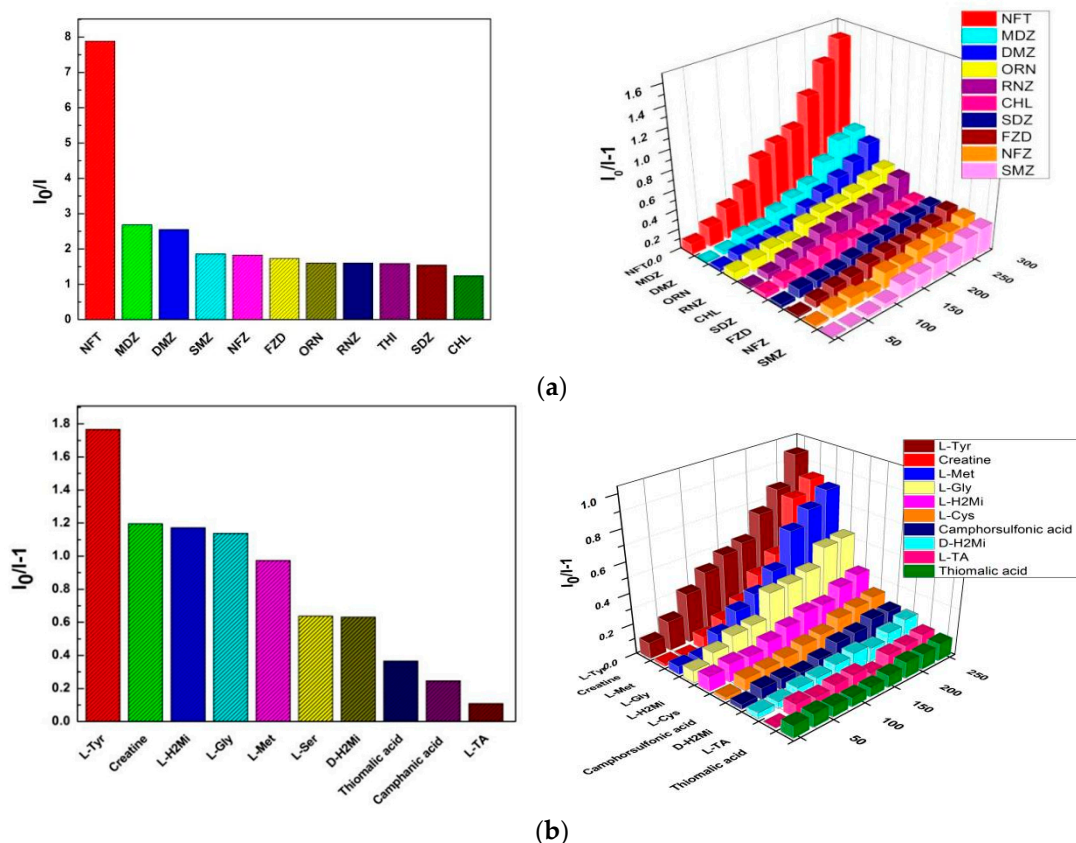


**Figure 4.** (a) Photo-luminescent intensities at 353 nm for **1** in the presence of different antibiotics; (b) photo-luminescent intensities at 353 nm for **1** in the presence of different amino acids.

On the other hand, diverse amino acids were added into the suspensions of **1** to study the photo-luminescence response of **1**. Different amino acids, including L-tyrosine (L-Tyr), creatine, L-malic acid(L-H<sub>2</sub>MI), D-malic acid (D-H<sub>2</sub>MI), L-methionine (L-Met), L-glycine(L-Gly), L-cysteine (L-Cys), camphorsulfonic acid, L-tartaric acid(L-TA) and thiomalic acid were studied. As shown in Figure 4b, L-Tyr showed the most obvious fluorescence quenching result. The fluorescence emission intensities of **1** are highly depended on the addition of L-Tyr, indicating that **1** could be used as the fluorescence probe of L-Tyr.

The Stern–Volmer (SV) curves for NFT and L-Tyr were plotted, respectively [79]. The SV curves of NFT and L-Tyr were approximately linear in the concentration range of 0–0.54 and 0–0.6 mM, respectively.  $I_0/I = K_{SV}[A] + 1$  was used to determine the value of  $K_{SV}$ , in which  $I$  and  $I_0$  represent the emission intensities with or without NFT or L-Tyr,  $[A]$  is the concentration of NFT or L-Tyr, and  $K_{SV}$  is the quenching coefficient. The detection limit of NFT/L-Tyr is 17.0/3.6  $\mu\text{M}$  and  $K_{SV}$  is  $3.0 \times 10^3/1.4 \times 10^4 \text{ M}^{-1}$  (Figure 5). The PXRD patterns of **1** immersed in the ethanol solution of NFT or L-Tyr for 24 h are in good agreement with the simulated PXRD of **1**, indicating the structure of **1** did not collapse in the detection process (Figure S5, Supplementary Materials). Therefore, **1** is a good candidate as a fluorescence probe for NFT or L-Tyr.

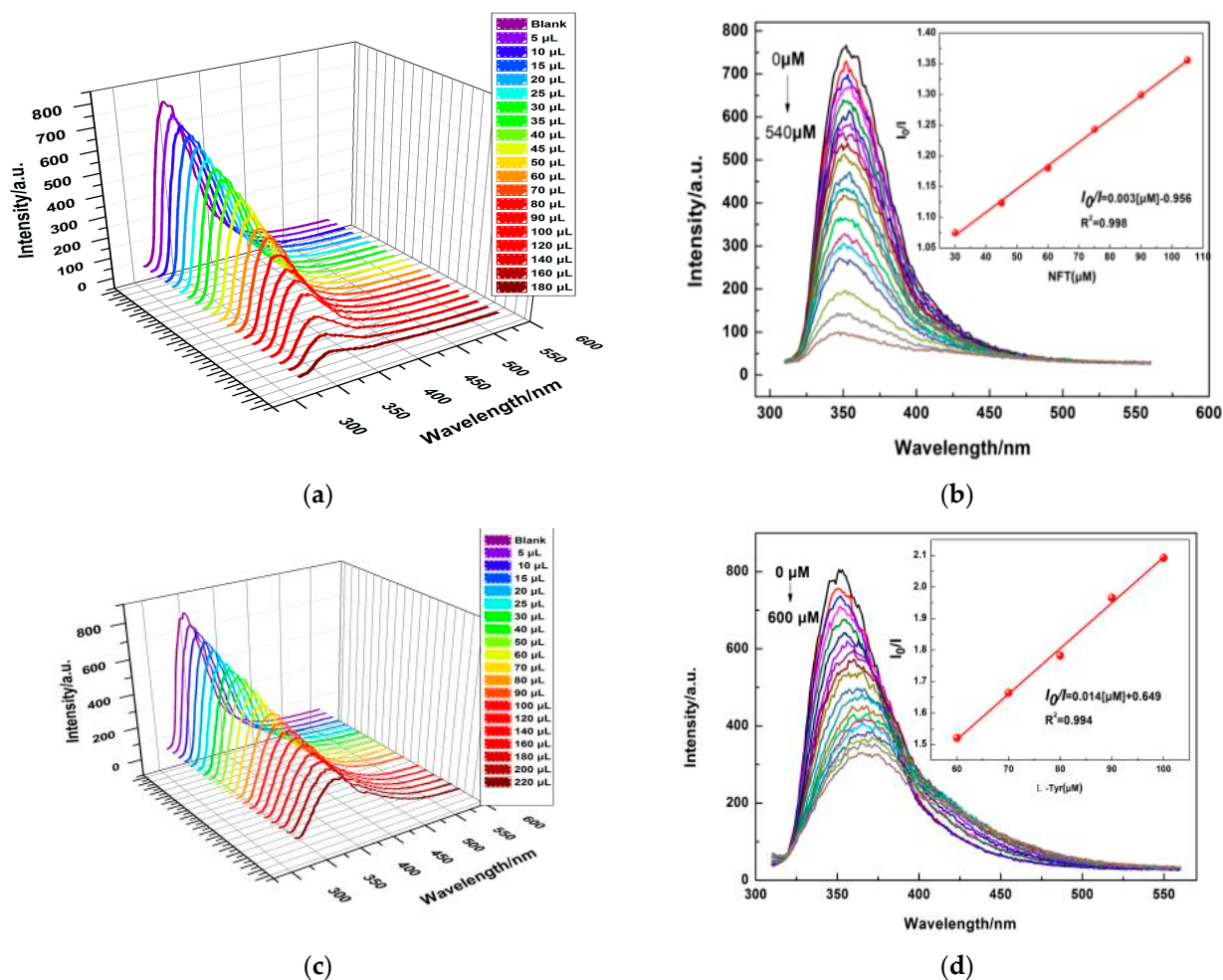


**Figure 5.** (a) The luminescence spectra of **1** with different concentrations of NFT; (b) The emission spectra by adding different concentration NFT buffer excited at 300 nm; (c) The luminescence spectra of **1** under different concentrations of L-Tyr; (d) The emission spectra by adding different concentration L-Tyr buffer excited at 300 nm.

Fluorescence lifetime is an important parameter for judging the mechanism of fluorescence quenching [80]. We investigated the fluorescence lifetimes for the suspensions of **1** with the addition of NFT or L-Tyr at room temperature, as shown in Figure 6 and Table 1. When NFT or L-Tyr was added into the suspensions of **1**, the fluorescence lifetimes change from 4.44 ns to 4.77 ns or 2.82 ns, indicating the existence of a dynamic fluorescent quenching mechanism. The results also suggested that NFT and L-Tyr may interact with **1** through weak interactions such as hydrogen bonding interactions. Considering that the photo-luminescent origin of **1** is from ligand-based luminescent emission and the 2D coordination framework of **1** have uncoordinated tetrazole moieties of  $HL^-$ , these uncoordinated tetrazole moieties could have hydrogen bonding interactions with the analytic species, which can reduce the photo-luminescent emission of **1** and cause the dynamic quenching phenomenon [81].

We also investigated the cycling performance of **1** (Figure 7). After four cycles, the efficiency of NFT or L-Tyr was 62.98 or 76.48%, indicating medium cycling performance.

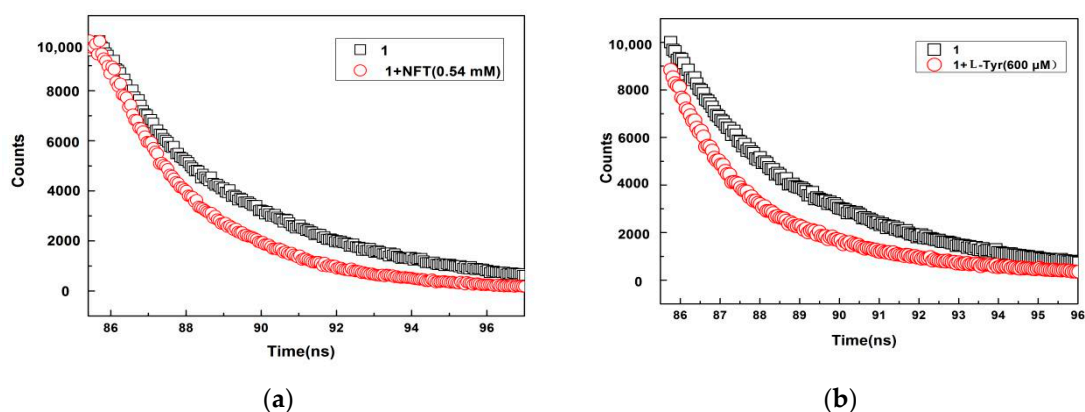
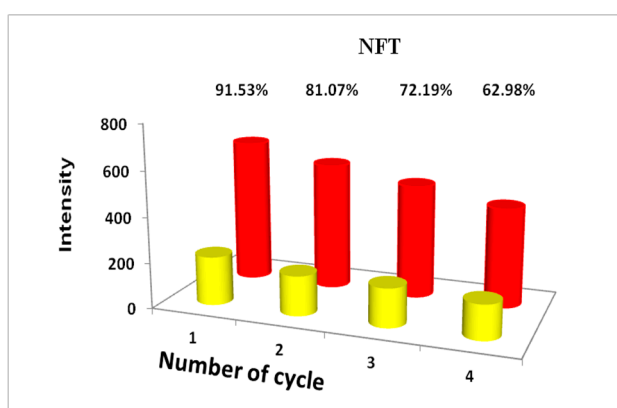


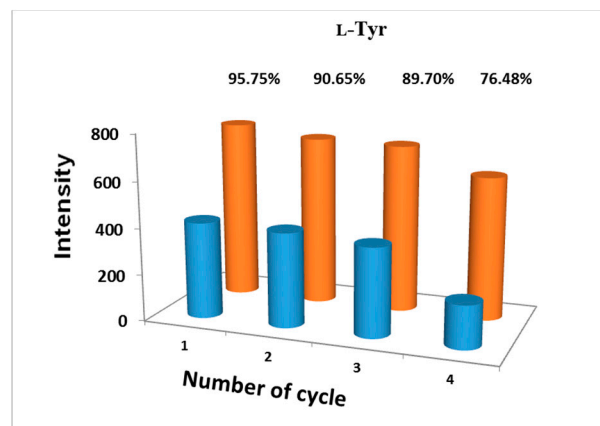
Figure 6. (a) The decay curve of 1 with the addition of NFT; (b) The decay curve of 1 with the addition of L-Tyr.

Table 1. The lifetimes of 1 with or without the addition of NFT and L-Tyr.

Caption	T <sub>1</sub> /ns	T <sub>2</sub> /ns	B <sub>1</sub> /%	B <sub>2</sub> /%	Combined Life Rating/ns
1	3.487773	6.584965	69.38	30.62	4.436
1 + NFT	1.997302	3.409927	41.78	58.22	2.820
1 + L-Tyr	2.528950	10.37314	71.39	28.61	4.773



(a)



(b)

Figure 7. Cycling performance of luminescence intensities at 300 nm of 1 for detecting NFT (a) and L-Tyr (b).

### 3. Materials and Methods

#### 3.1. General Remarks

H<sub>3</sub>L was purchased from Jinan Henghua Technology Co., Ltd., Shan Dong, China. All other chemicals were purchased commercially and applied directly. Perkin-Elmer 240 element analyzer (PerkinElmer, Dublin, Ireland) is used for microanalysis of C, H and N elements. The ultraviolet-visible spectrophotometer (model UV-2600) manufactured by Shimadzu Company (Shimadzu, Kyoto, Japan), was used to measure the absorption spectra at room temperature, with the test wavelength ranging from 200–800 nm. Powder X-ray diffraction analysis was characterized by Rigaku D/Max-2500 (Rigaku, Tokyo, Japan) X-ray diffractometer equipped with Cu-K $\alpha$  radiation at a wavelength of 0.154 nm. Photo-luminescence lifetimes and solid-state fluorescence spectra were measured by FS5 fluorescence spectrometer (Edinburgh Instruments, Edinburgh, UK). The RF-5301 fluorescence spectrophotometer (Shimadzu, Kyoto, Japan) was used to carry out the photo-luminescence sensing experiment, equipped with a plotter unit and 1 cm  $\times$  1 cm quartz battery in phosphorescent mode.



### 3.2. Preparation of $[La(HL)(DMF)_2(NO_3)]$ (**1**)

$La(NO_3)_2 \cdot 6H_2O$  (129.9 mg, 0.3 mmol),  $H_3L$  (31.0 mg, 0.1 mmol), ethanol (3 mL) and DMF (1 mL) were added to a beaker and stirred for 0.5 h, and then the mixture was transferred to a steel high-pressure reaction kettle which is heated to 90 °C for 72 h, and cooled to the ambient temperature within 36 h. The resulting pale yellow powder was cleaned with ethanol several times (Scheme 2). At room temperature, the powder of **1** was evenly distributed in ethanol solution with a concentration of 0.1 mg/mL by the ultrasonic method, which was used for further fluorescent measurement. Yield: 36% based on  $H_3L$ . Elemental analysis calculations (%) for  $C_{21}H_{22}LaN_7O_9$ : C 38.49, H 3.38, N 14.96; Found: C 38.57, H 3.49, N 15.13. FT-IR data ( $cm^{-1}$ , KBr): 3412(w), 1649(m), 1621(m), 1584(w), 1500(w), 1449(w), 1421(w), 1384(s), 1296(w), 1112(w), 779(w), 719(w), 674(w). The prepared sample needs to be pretreated before FT-IR and other characterization.



**Scheme 2.** Synthesis route for **1**.

### 3.3. X-ray Crystallography

The Bruker SMART 1000 CCD diffractometer (Bruker, AVANCE, Billerica, MA, USA) was used to measure the diffraction data of a single crystal of **1**, equipped with graphite monochromatic Mo-K $\alpha$  aperture radiation ( $\lambda = 0.71073$  Å). The  $\omega$ - $\phi$  scanning strategy was applied with Lorentz polarization and empirical absorption correction. By utilizing the SHELXS97 program, the structure of **1** was improved by utilizing a full matrix least squares calculation. The anisotropic temperature factor was assigned to all atoms except hydrogen atoms, and the isotropic temperature factor was arbitrarily selected to be 1.2 times that of the parent [82,83]. The R(F), WR(F<sup>2</sup>) and goodness of fit protocol factors, details of data collection and analysis are shown in Table 2. The selected bond lengths, angle hydrogen bonds [Å] and angles [°] are given in Table S1, Supplementary Materials. CCDC-1873742 represents the crystal data for this work. The data is available free of charge through the Cambridge Crystal Data Center.

**Table 2.** Crystal Data and Structure Refinement Information for **1**.

<b>1</b>	
Formula	$C_{21}H_{22}LaN_7O_9$
$M$ ( $g \cdot mol^{-1}$ )	655.36
Crystal system	Monoclinic
Space group	$C2/c$
Temperature	133.32(16)
$a$ (Å)	28.2179(10)
$b$ (Å)	14.0169(5)
$c$ (Å)	14.3437(5)
$\alpha$ (°)	90
$\beta$ (°)	99.720(4)

Table 2. Cont.

1	
$\gamma$ (°)	90
$V$ (Å <sup>3</sup> )	5591.9(3)
$Z$	8
$F$ (000)	2608
$\rho_{\text{calc}}$ (Mg·m <sup>-3</sup> )	1.557
$\mu$ (mm <sup>-1</sup> )	1.586
Data/restraints/parameters	4916/36/362
GOF on $F^2$	1.069
$R_1$ <sup>a</sup> ( $I \geq 2\sigma(I)$ )	0.0273
$wR_2$ <sup>b</sup> (all data)	0.0643

$$^a R_1 = \sum ||F_o| - |F_c|| / \sum |F_o|, ^b wR_2 = [\sum w(F_o^2 - F_c^2)^2 / \sum w(F_o^2)^2]^{1/2}.$$

#### 4. Conclusions

In summary, the preparation, structural characterization and photo-luminescent sensing performance of a 2D lanthanide metal-organic framework was reported. It can be utilized to detect trace nitrofurantoin ( $K_{sv}$ :  $3.0 \times 10^3 \text{ M}^{-1}$  and detection limit:  $17.0 \mu\text{M}$ ) and L-tyrosine ( $K_{sv}$ :  $1.4 \times 10^4 \text{ M}^{-1}$  and detection limit:  $3.6 \mu\text{M}$ ) with high sensitivity and good recyclability. This work not only enriches the research of lanthanide MOFs, but also provides a theoretical basis for 2D MOF-based chemical sensors.

**Supplementary Materials:** Table S1: Selected bond lengths (Å) and angles (°), Figure S1: FT-IR spectrum of **1**, Figure S2: (a) The SEM images of H<sub>2</sub>L showed that the powder is needle-like with the length between 0.54–5.99  $\mu\text{m}$  at a scale of 5  $\mu\text{m}$  (b) The SEM images of H<sub>2</sub>L showed that the powder is acicular on a 2  $\mu\text{m}$  scale., Figure S3: UV-Vis spectra of H<sub>3</sub>L and **1**, Figure S4: Solid-state fluorescence of H<sub>3</sub>L and **1**, Figure S5: powder X-ray patterns for **1**, **1** + NFT and **1** + L-Tyr.

**Author Contributions:** Conceptualization, B.D.; data collocation and analysis, T.-T.W., J.-Y.L., J.-D.A. and Y.-Y.L.; Validation, R.G. and J.-Z.H.; Writing—original draft, T.-T.W.; Writing—review and editing, W.S. and B.D. All authors have read and agreed to the published version of the manuscript.

**Funding:** This work was financially supported by the National Natural Science Foundation of China (21931004), the Natural Science Foundation of Tianjin (18JCJQJC47200), the Ministry of Education of China (B12015) and the Natural Science Foundation of the Science and Technology Development Fund of Tianjin Education Commission for Higher Education (2019ZD15).

**Data Availability Statement:** The data presented in this study are available with the authors.

**Acknowledgments:** The authors are grateful to Tianjin Normal University and Nankai University for the necessary research works and instruments.

**Conflicts of Interest:** The authors declare no conflict of interest.

**Sample Availability:** Sample of the compound **1** is available from the authors.

#### References

- Calahorra, A.J.; Briones, D.; Seco, J.M.; Salinas-Castillo, A.; Rodriguez-Dieguez, A.; Mendicutie-Fierro, C. Bidimensional cadmium metal-organic frameworks based on 1,3-bis(4-pyridyl)propane displaying long lifetime photoluminescence emission. *Polyhedron* **2015**, *91*, 47–51. [CrossRef]
- Al-Janabi, N.; Deng, H.R.; Borges, J.; Liu, X.F.; Garforth, A.; Siperstein, F.R.; Fan, X.L. A facile post-synthetic modification method to improve hydrothermal stability and CO<sub>2</sub> selectivity of CuBTC metal-organic framework. *Ind. Eng. Chem.* **2016**, *55*, 7941–7949. [CrossRef]
- Masoomi, M.Y.; Morsali, A.; Dhakshinamoorthy, A.; Garcia, H. Mixed-metal MOFs: Unique opportunities in metal-organic framework (MOF) functionality and design. *Angew. Chem. Int. Ed.* **2019**, *58*, 15188–15205. [CrossRef]
- Li, J.-R.; Kuppler, R.-J.; Zhou, H.-C. Selective gas adsorption and separation in metal-organic frameworks. *Chem. Soc. Rev.* **2009**, *38*, 1477–1504. [CrossRef] [PubMed]
- Carter, K.P.; Young, A.E.; Palmer, A.E. Fluorescent sensors for measuring metal ions in living systems. *Chem. Rev.* **2014**, *114*, 4564–4601. [CrossRef] [PubMed]

6. Simagina, A.A.; Polynski, M.V.; Vinogradov, A.V.; Pidko, E.A. Towards rational design of metal-organic framework-based drug delivery systems. *Russ. Chem. Rev.* **2018**, *87*, 831–858. [[CrossRef](#)]
7. Lysova, A.A.; Samsonenko, D.G.; Kovalenko, K.A.; Nizovtsev, A.S.; Dybtsev, D.N.; Fedin, V.P. A Series of Mesoporous Metal-Organic Frameworks with Tunable Windows Sizes and Exceptionally High Ethane over Ethylene Adsorption Selectivity. *Angew. Chem. Int. Ed.* **2020**, *59*, 20561–20567. [[CrossRef](#)] [[PubMed](#)]
8. Sopianik, A.A.; Kovalenko, K.A.; Samsonenko, D.G.; Barsukova, M.O.; Dybtsev, D.N.; Fedin, V.P. Exceptionally effective benzene/cyclohexane separation using a nitro-decorated metal-organic framework. *Chem. Commun.* **2020**, *56*, 8241–8244. [[CrossRef](#)] [[PubMed](#)]
9. Sopianik, A.A.; Fedin, V.P. Main Approaches to the Synthesis of Heterometallic Metal-Organic Frameworks. *Russ. J. Coord. Chem.* **2020**, *46*, 443–457. [[CrossRef](#)]
10. Lustig, W.P.; Mukherjee, S.; Rudd, N.D.; Desai, A.V.; Li, J.; Ghosh, S.K. Metal-organic frameworks: Functional luminescent and photonic materials for sensing applications. *Chem. Soc. Rev.* **2017**, *46*, 3242–3285. [[CrossRef](#)]
11. Meng, J.-S.; Liu, X.; Niu, C.-J.; Pang, Q.; Li, J.-T.; Liu, F.; Liu, Z.; Mai, L.-Q. Advances in metal-organic framework coatings: Versatile synthesis and broad applications. *Chem. Soc. Rev.* **2020**, *49*, 3142–3186. [[CrossRef](#)]
12. Chen, K.; Wu, C.-D. Development of photoluminescence metal-organic framework sensors consisting of dual-emission centers. *Chin. Chem. Lett.* **2019**, *29*, 823–826. [[CrossRef](#)]
13. Lysova, A.A.; Samsonenko, D.G.; Dorovatovskii, P.V.; Lazarenko, V.A.; Khrustalev, V.N.; Kovalenko, K.A.; Dybtsev, D.N.; Fedin, V.P. Tuning the Molecular and Cationic Affinity in a Series of Multifunctional Metal-Organic Frameworks Based on Dodecanuclear Zn(II) Carboxylate Wheels. *J. Am. Chem. Soc.* **2019**, *141*, 17260–17269. [[CrossRef](#)] [[PubMed](#)]
14. Wu, S.-Y.; Min, H.; Shi, W.; Cheng, P. Multicenter Metal-Organic Framework-Based Ratiometric Fluorescent Sensors. *Adv. Mater.* **2020**, *32*, 1805871. [[CrossRef](#)]
15. Han, Z.-S.; Wang, K.-Y.; Guo, Y.-F.; Chen, W.-J.; Zhang, J.-L.; Zhang, X.-R.; Siligard, G.; Yang, S.-H.; Zhou, Z.; Sun, P.-C.; et al. Cation-induced chirality in a bifunctional metal-organic framework for quantitative enantioselective recognition. *Nat. Commun.* **2019**, *10*, 5117. [[CrossRef](#)]
16. Zhang, S.-Y.; Wang, Z.-Y.; Gao, J.; Wang, K.-Y.; Gianolio, E.; Aime, S.; Shi, W.; Zhou, Z.; Cheng, P.; Zaworotko, M.J. A Gadolinium(III) Zeolite-like Metal-Organic-Framework-Based Magnetic Resonance Thermometer. *Chem* **2019**, *5*, 1609–1618. [[CrossRef](#)]
17. Wang, D.-B.; Tan, Q.-H.; Liu, J.-J.; Liu, Z.-L. A stable europium metal-organic framework as a dual-functional luminescent sensor for quantitatively detecting temperature and humidity. *Dalton Trans.* **2016**, *45*, 18450–18454. [[CrossRef](#)] [[PubMed](#)]
18. Chen, Z.-H.; Han, Z.-S.; Shi, W.; Cheng, P. Design, Synthesis and Applications of Chiral Metal-Organic Frameworks. *Acta Chim. Sin.* **2020**, *78*, 1336–1348. [[CrossRef](#)]
19. Hou, Y.-L.; Xu, H.; Cheng, Q.-Q.; Zhao, B. Controlled lanthanide-organic framework nanospheres as reversible and sensitive luminescent sensors for practical applications. *Chem. Commun.* **2015**, *51*, 6769–6772. [[CrossRef](#)]
20. Dong, M.-J.; Zhao, M.; Ou, S.; Zou, C.; Wu, C.-D. A luminescent Dye@MOF platform: Emission fingerprint relationships of volatile organic molecules. *Angew. Chem. Int. Ed.* **2014**, *53*, 1575–1579. [[CrossRef](#)]
21. Xiong, J.; Yang, L.; Gao, L.-X.; Zhu, P.-P.; Chen, Q.; Tan, K.-J. A highly fluorescent lanthanide metal-organic framework as dual-mode visual sensor for berberine hydrochloride and tetracycline. *Anal. Bioanal. Chem.* **2019**, *411*, 5963–5973. [[CrossRef](#)]
22. Lian, X.; Yan, B. A lanthanide metal-organic framework (MOF-76) for adsorbing dyes and fluorescence detecting aromatic pollutants. *RSC Adv.* **2016**, *6*, 11570–11576. [[CrossRef](#)]
23. Wenciewicz, T.A. Crossroads of antibiotic resistance and biosynthesis. *J. Mol. Biol.* **2016**, *431*, 3370–3399. [[CrossRef](#)] [[PubMed](#)]
24. Ruppe, E.; Burdet, C.; Grall, N.; Lastours, V.; Lescure, F.X.; Andreumont, A.; Armand-Lefevre, L. Impact of antibiotics on the intestinal microbiota needs to be re-defined to optimize antibiotic usage. *Clin. Microbiol. Infect.* **2018**, *24*, 783–784. [[CrossRef](#)]
25. Pruden, A.; Pei, R.-T.; Storteboom, H. Antibiotic resistance genes as emerging contaminants: Studies in Northern Colorado. *Environ. Sci. Technol.* **2006**, *40*, 7445–7450. [[CrossRef](#)] [[PubMed](#)]
26. Jager, L.P.; Graaf, G.J.; Widjaja-Greefkes, H.C.A. Effects of alpha(1)-antagonists on production and release of aldosterone and other steroid hormones by porcine adrenocortical cells in vitro. *Can. J. Physiol. Pharm.* **1998**, *76*, 676–683. [[CrossRef](#)]
27. McEvoy, J.D.G. Contamination of animal feedingstuffs as a cause of residues in food: A review of regulatory aspects, incidence and control. *Anal. Chim. Acta* **2002**, *473*, 3–26. [[CrossRef](#)]
28. Available online: [http://www.moa.gov.cn/nybg/b/2008/djiuq/201806/t20180611\\_6151661.htm](http://www.moa.gov.cn/nybg/b/2008/djiuq/201806/t20180611_6151661.htm) (accessed on 14 May 2021).
29. Kalser, L.R.; Robr, F.J.; Koron, M.S.; Levy, H.L. Tyrosine supplementation in phenylketonuria: Diurnal blood tyrosine levels and presumptive brain influx of tyrosine and other large neutral amino acids. *J. Pediatr.* **2001**, *139*, 421–427. [[CrossRef](#)]
30. Rohr, F.J.; Lobbregt, D.; Levy, H.L. Tyrosine supplementation in the treatment of maternal phenylketonuria. *Am. J. Clin. Nutr.* **1998**, *67*, 473–476. [[CrossRef](#)]
31. Smith, M.L.; Hanley, W.B.; Clarke, J.T.R.; Klim, P.; Schoonheydt, W.; Austin, V.; Lehotay, D.C. Randomised controlled trial of tyrosine supplementation on neuropsychological performance in phenylketonuria. *Arch. Dis. Child.* **1998**, *78*, 116–121. [[CrossRef](#)]
32. Levy, P.A.; Miller, J.B.; Shapira, E. The advantage of phenylalanine to tyrosine ratio for the early detection of phenylketonuria. *Clin. Chim. Acta* **1998**, *270*, 177–181. [[CrossRef](#)]
33. Mcardle, L.; Rafferty, M.; Maelandsmo, G.M.; Bergin, O.; Farr, C.J.; Dervan, P.A.; O'Loughlin, S.; Herlyn, M.; Easty, D.J. Protein tyrosine phosphatase genes downregulated in melanoma. *J. Investig. Dermatol.* **2001**, *117*, 1255–1260. [[CrossRef](#)]

34. Buron, G.; Hacquemand, R.; Pourie, G.; Brand, G. Inhalation exposure to acetone induces selective damage on olfactory neuroepithelium in mice. *Neurotoxicology* **2009**, *30*, 114–120. [[CrossRef](#)] [[PubMed](#)]
35. Kumarvel, V.; Da Fonseca, J. Acetone poisoning—a diagnostic dilemma. *Eur. J. Anaesthesiol.* **2007**, *24*, 805–806. [[CrossRef](#)]
36. Pak, Y.L.; Swamy, K.M.K.; Yoon, J. Recent Progress in Fluorescent Imaging Probes. *Sensors* **2015**, *15*, 24374–24396. [[CrossRef](#)]
37. Clementino, R.F.P.; Santos, A.B.D.; Marques, O.J.B.J.; Ratkovski, D.R.; Gatto, C.C.; Malvestiti, I.; Machado, F.L.D.; Falcao, E.H.L. Structural description, luminescent and magnetic properties of novel 2-D coordination polymers containing thiazolo[5,4-d]thiazole rings and trivalent lanthanide ions. *J. Solid State Chem.* **2018**, *268*, 94–101. [[CrossRef](#)]
38. Kostakis, G.E.; Ako, A.M.; Powell, A.K. Structural motifs and topological representation of Mn coordination clusters. *Chem. Soc. Rev.* **2010**, *39*, 2238–2271. [[CrossRef](#)] [[PubMed](#)]
39. Tabacaru, A.; Pettinari, C.; Galli, S. Coordination polymers and metal-organic frameworks built up with poly(tetrazolate) ligands. *Coord. Chem. Rev.* **2018**, *372*, 1–30. [[CrossRef](#)]
40. Putnam, C.D.; Hammel, M.; Hura, G.L.; Tainer, J.A. X-ray solution scattering (SAXS) combined with crystallography and computation: Defining accurate macromolecular structures, conformations and assemblies in solution. *Q. Rev. Biophys.* **2007**, *40*, 191–285. [[CrossRef](#)] [[PubMed](#)]
41. Cai, Z.-Y.; Zhu, H.-X.; Wang, P.; Wu, C.-Y.; Gao, W.-C.; Mu, J.-Y.; Wei, S.-Y. Performance optimization of UV curable waterborne polyurethane acrylate wood coatings modified by castor oil. *J. For. Eng.* **2020**, *5*, 89–95.
42. Zheng, C.-X.; Zhu, S.-L.; Lu, Y.; Mei, C.-T.; Xu, X.-W.; Yue, Y.-Y.; Han, J.-Q. Synthesis and characterization of cellulose nanofibers/polyacrylic acid-polyacrylamide double network electroconductive hydrogel. *J. For. Eng.* **2020**, *5*, 93–100.
43. Ibitoye, S.E.; Adegun, I.K.; Omoniyi, P.O.; Ogedengbe, T.S.; Alabi, O.O. Numerical investigation of thermo-physical properties of non-newtonian fluid in a modelled intestine. *J. Bioresour. Bioprod.* **2020**, *5*, 211–221. [[CrossRef](#)]
44. Tan, W.; Hao, X.-L.; Wang, Q.-W.; Ou, R.-X. Mechanical and thermal properties of bamboo plastic composites reinforced by thermotropic liquid crystal copolyesters. *J. For. Eng.* **2020**, *5*, 97–103.
45. Zhu, L.-T.; Gu, Y.-F.; Wu, G.-S. Biomass thermal conductivity measurement system design. *J. For. Eng.* **2020**, *5*, 97–102.
46. Krishnakumar, V.; Xavier, R.J. FT Raman and FT-IR spectral studies of 3-mercapto-1,2,4-triazole. *Spectrochim. Acta A* **2004**, *60*, 709–714. [[CrossRef](#)]
47. Cao, Y.; Wang, X.-Z.; Li, Y.-J.; Shen, D.-H.; Dai, Y.-P.; Zhang, S.-Z.; Zhang, W.-G. Effect of high temperature oil heat treatment on the starch content and mold-resistant property of bamboo. *J. For. Eng.* **2020**, *5*, 109–115.
48. Zhang, M.-J.; Ma, W.-J.; Cui, J.-X.; Wu, S.-T.; Han, J.-Q.; Zou, Y.; Huang, C.-B. Hydrothermal synthesized UV-resistance and transparent coating composited superoleophilic electrospun membrane for high efficiency oily wastewater treatment. *J. Hazard. Mater.* **2020**, *383*, 121152. [[CrossRef](#)] [[PubMed](#)]
49. Lv, D.; Wang, R.-X.; Tang, G.-S.; Mou, Z.-P.; Lei, J.-D.; Han, J.-Q.; Smedt, S.D.; Xiong, R.-H.; Huang, C.-B. Ecofriendly electrospun membranes loaded with visible-lightresponding nanoparticles for multifunctional usages: Highly efficient air filtration, dye scavenging, and bactericidal activity. *ACS Appl. Mater. Interfaces* **2019**, *11*, 12880–12889. [[CrossRef](#)]
50. Zhu, M.-M.; Xiong, R.-H.; Huang, C.-B. Bio-Based and Photocrosslinked Electrospun Antibacterial Nanofibrous Membranes for Air Filtration. *Carbohydr. Polym.* **2019**, *205*, 55–62. [[CrossRef](#)]
51. Tang, G.-S.; Chen, L.; Wang, Z.-X.; Gao, S.-T.; Qu, Q.-L.; Xiong, R.-H.; Braeckmans, K.; Smedt, S.C.D.; Zhang, Y.-S.; Huang, C.-B. Faithful Fabrication of Biocompatible Multicompartmental Memomicrospheres for Digitally Color-Tunable Barcoding. *Small* **2020**, *16*, 1907586. [[CrossRef](#)]
52. Zhang, H.-Y.; Hua, D.-W.; Huang, C.-B.; Samal, S.K.; Xiong, R.-H.; Sauvage, F.; Braeckmans, K.; Remaut, K.; Smedt, S.C.D. Materials and Technologies to Combat Counterfeiting of Pharmaceuticals: Current and Future Problem Tackling. *Adv. Mater.* **2020**, *32*, 1905486. [[CrossRef](#)]
53. Tang, G.-S.; Chen, L.; Lian, L.-M.; Li, F.-H.; Ravanbakhsh, H.; Wang, M.; Zhang, Y.-S.; Huang, C.-B. Designable dual-power micromotors fabricated from a biocompatible gas-shearing strategy. *Chem. Eng. J.* **2021**, *407*, 127187. [[CrossRef](#)]
54. Hua, D.-W.; Gao, S.-T.; Zhang, M.-J.; Ma, W.-J.; Huang, C.-B. A Novel Xanthan Gum-Based Conductive Hydrogel with Excellent Mechanical, Biocompatible, and Self-Healing Performances. *Carbohydr. Polym.* **2020**, *247*, 116743. [[CrossRef](#)]
55. Xiong, R.-H.; Xu, R.-X.; Huang, C.-B.; Smedt, S.D.; Braeckmans, K. Stimuli-responsive nanobubbles for biomedical applications. *Chem. Soc. Rev.* **2021**, *50*, 5746–5776. [[CrossRef](#)] [[PubMed](#)]
56. Tang, G.-S.; Xiong, R.-H.; Lv, D.; Xu, R.-X.; Braeckmans, K.; Huang, C.-B.; Smedt, S.C.D. Gas-Shearing Fabrication of Multicompartmental Microspheres: A One-Step and Oil-Free Approach. *Adv. Sci.* **2019**, *6*, 1802342–1802351. [[CrossRef](#)]
57. An, J.; Kim, S.; Shrinidhi, A.; Kim, J.; Banna, H.; Sung, G.H.; Park, K.M.; Kim, K. Purification of protein therapeutics via high-affinity supramolecular host-guest interactions. *Nat. Biomed. Eng.* **2020**, *4*, 1044. [[CrossRef](#)] [[PubMed](#)]
58. Gao, S.-T.; Tang, G.-S.; Hua, D.-W.; Xiong, R.-H.; Han, J.-Q.; Jiang, S.-H.; Zhang, Q.-L.; Huang, C.-B. Stimuli-responsive bio-based polymeric systems and their applications. *J. Mater. Chem. B.* **2019**, *7*, 709–729. [[CrossRef](#)]
59. Hwang, W.; Yoo, J.; Hwang, I.; Lee, J.; Ko, Y.H.; Kim, H.W.; Kim, Y.; Lee, Y.; Hur, M.Y.; Park, K.M.; et al. Hierarchical Self-assembly of Polypseudorotaxanes into Artificial Microtubules. *Angew. Chem. Int. Ed.* **2020**, *59*, 3460–3464. [[CrossRef](#)]
60. Hua, D.-W.; Xiong, R.-H.; Braeckmans, K.; Scheid, B.; Huang, C.-B.; Sauvage, F.; Smedt, S.C.D. Concentration Gradients in Material Sciences: Methods to Design and Biomedical Applications. *Adv. Funct. Mater.* **2021**, *31*, 2009005. [[CrossRef](#)]
61. Zhang, M.-M.; Ma, W.-J.; Wu, S.-T.; Tang, G.-S.; Cui, J.-X.; Zhang, Q.-L.; Chen, F.; Xiong, R.-H.; Huang, C.-B. Electrospun frogspawn structured membrane for gravity-driven oil-water separation. *J. Colloid Interface Sci.* **2019**, *547*, 136–144. [[CrossRef](#)]

62. Cui, J.-X.; Lu, T.; Li, F.-H.; Wang, Y.-L.; Lei, J.-D.; Ma, W.-J.; Zou, Y.; Huang, C.-B. Flexible and transparent composite nanofibre membrane that was fabricated via a “green” electrospinning method for efficient particulate matter 2.5 capture. *J. Colloid Interface Sci.* **2021**, *582*, 506–514. [[CrossRef](#)]
63. Lv, D.; Tang, G.-S.; Chen, L.; Zhang, M.-J.; Cui, J.-X.; Xiong, R.-H.; Huang, C.-B. Multifunctional Gas-Spinning Hierarchical Architecture: A Robust and Efficient Nanofiber Membrane for Simultaneous Air and Water Contaminant Remediation. *ACS Appl. Polym. Mater.* **2020**, *2*, 5686–5697. [[CrossRef](#)]
64. Yorseng, K.; Siengchin, S.; Ashok, B.; Rajulu, A.V. Nanocomposite egg shell powder with in situ generated silver nanoparticles using inherent collagen as reducing agent. *J. Bioresour. Bioprod.* **2020**, *5*, 101–107. [[CrossRef](#)]
65. Ashok, B.; Hariram, N.; Siengchin, S.; Rajulu, A.V. Modification of tamarind fruit shell powder with in situ generated copper nanoparticles by single step hydrothermal method. *J. Bioresour. Bioprod.* **2020**, *5*, 180–185. [[CrossRef](#)]
66. Shultz, A.M.; Sarjeant, A.A.; Farha, O.K.; Hupp, J.T.; Nguyen, S.T. Post-Synthesis Modification of a Metal-Organic Framework to Form Metallosalen-Containing MOF Materials. *J. Am. Chem. Soc.* **2011**, *133*, 13252–13255. [[CrossRef](#)]
67. Qu, Q.-L.; Zhang, J.; Chen, X.-Q.; Ravanbakhsh, H.; Tang, G.-S.; Xiong, R.-H.; Manshian, B.-B.; Soenen, S.-J.; Sauvage, F.; Braeckmans, K.; et al. Triggered Release from Cellulose Microparticles Inspired by Wood Degradation by Fungi. *ACS Sustain. Chem. Eng.* **2021**, *9*, 387–397. [[CrossRef](#)]
68. Zhang, Y.-Y.; Zhao, Y.-L.; Song, B.; Huang, C.-B. Spectroscopic behavior and intracellular application of a highly sensitive UV-fluorescence double ratio probe based on water-soluble indole for detection acid pH. *Dyes Pigments* **2021**, *188*, 109205. [[CrossRef](#)]
69. Zhang, M.; Feng, G.X.; Song, Z.G.; Zhou, Y.P.; Chao, H.Y.; Yuan, D.Q.; Tan, T.T.Y.; Guo, Z.G.; Hu, Z.G.; Tang, B.Z.; et al. Two-Dimensional Metal-Organic Framework with Wide Channels and Responsive Turn-On Fluorescence for the Chemical Sensing of Volatile Organic Compounds. *J. Am. Chem. Soc.* **2014**, *136*, 7241–7244. [[CrossRef](#)] [[PubMed](#)]
70. Yang, L.; Song, Y.-H.; Wang, L. Multi-emission metal-organic framework composites for multicomponent ratiometric fluorescence sensing: Recent developments and future challenges. *J. Mater. Chem. B* **2020**, *8*, 3292–3315. [[CrossRef](#)] [[PubMed](#)]
71. Li, F.-Y.; Chen, D.-X.; Wu, M.-K.; Han, L.; Jiang, H.-L. Chemical Sensors Based on Metal-Organic Frameworks. *Chem. Plus. Chem.* **2016**, *81*, 675–690.
72. Allendorf, M.D.; Bauer, C.A.; Bhakta, R.K.; Houk, R.J.T. Luminescent metal-organic frameworks. *Chem. Soc. Rev.* **2009**, *38*, 1330–1352. [[CrossRef](#)]
73. Calvez, G.; Le Natur, F.; Daiguebonne, C.; Bernot, K.; Suffren, Y.; Guillou, O. Lanthanide-based hexa-nuclear complexes and their use as molecular precursors. *Coord. Chem. Rev.* **2017**, *340*, 134–153. [[CrossRef](#)]
74. Zhang, Y.-Y.; Zhao, Y.-L.; Wu, Y.-N.; Zhao, B.; Wang, L.-Y.; Song, B.; Huang, C.-B. Benzoinole-based bifunctional ratiometric turn-on sensor with an ICT effect for trapping of H<sup>+</sup> and Al<sup>3+</sup> in dual-channel cell imaging and samples. *Spectrochim. Acta A* **2021**, *247*, 119123. [[CrossRef](#)]
75. Cisse, L.; Djande, A.; Capo-Chichi, M.; Delattre, F.; Saba, A.; Brochon, J.C.; Sanouski, S.; Tine, A.; Aaron, J.J. Fluorescence Quenching of Two Coumarin-3-carboxylic Acids by Trivalent Lanthanide Ions. *J. Fluoresc.* **2017**, *27*, 619–628. [[CrossRef](#)]
76. Tarakanova, E.N.; Hamdoush, M.; Eroshin, A.V.; Ryzhov, I.V.; Zhabanov, Y.A.; Stuzhin, P.A. Preparation and Fluorescence Property of Metal-organic Framework Composite RhB/MOF-5. *Chem. J. Chin. Univ.* **2009**, *30*, 11–13.
77. Ying, Y.-M.; Tao, C.-L.; Yu, M.-X.; Xiong, Y.; Guo, C.-R.; Liu, X.-G.; Zhao, Z.-J. In situ encapsulation of pyridine-substituted tetraphenylethene cations in metal-organic framework for the detection of antibiotics in aqueous medium. *J. Mater. Chem. C* **2019**, *7*, 8383–8388. [[CrossRef](#)]
78. Zhang, H.Q.; Huang, Y.H.; Lin, X.H.; Lu, F.F.; Zhang, Z.S.; Hu, Z.B. Lanthanum loaded graphitic carbon nitride nanosheets for highly sensitive and selective fluorescent detection of iron ions. *Sens. Actuators B Chem.* **2018**, *255*, 2218–2222. [[CrossRef](#)]
79. Qin, C.-J.; Wang, W.-Y.; Wang, L.-X. A water-soluble organometallic conjugated polyelectrolyte for the direct colorimetric detection of silver ion in aqueous media with high selectivity and sensitivity. *Macromolecules* **2011**, *44*, 483–489. [[CrossRef](#)]
80. Li, P.; Guo, M.-Y.; Gao, L.-L.; Yin, X.-M.; Yang, S.-L.; Bu, R.; Gao, E.-Q. Photoresponsivity and antibiotic sensing properties of an entangled tris(pyridinium)-based metal-organic framework. *Dalton Trans.* **2020**, *49*, 7488–7495. [[CrossRef](#)]
81. Wang, Y.N.; Wang, S.D.; Cao, K.Z.; Zou, G.D. A dual-functional fluorescent Co(II) coordination polymer sensor for the selective sensing of ascorbic acid and acetylacetone. *J. Photochem. Photobiol. A* **2021**, *411*, 113204. [[CrossRef](#)]
82. Sheldrick, G.M. Crystal structure refinement with SHELXL. *Acta Crystallogr. Sect. C* **2015**, *71*, 3–8. [[CrossRef](#)] [[PubMed](#)]
83. Ma, T.Q.; Kapustin, E.A.; Yin, S.X.; Liang, L.; Zhou, Z.Y.; Niu, J.; Li, L.H.; Wang, Y.Y.; Su, J.; Li, J.; et al. Single-crystal x-ray diffraction structures of covalent organic frameworks. *Science* **2018**, *361*, 48–52. [[CrossRef](#)] [[PubMed](#)]